PAPER

Check for updates

Two-dimensional architecture of N,S-codoped nanocarbon composites embedding few-layer MoS₂ for efficient lithium storage†

Jintao Ren,‡ Dandan Yang, 🆔 ‡ Lei Chen and Zhong-Yong Yuan 🆔 *

The exploration and advancement of highly efficient anode materials for lithium-ion batteries (LIBs) are critical to meet the growing demands of the energy storage market. In this study, we present an easily scalable synthesis method for the one-pot formation of few-layer MoS₂ nanosheets on a N,S dual-doped carbon monolith with a two-dimensional (2D) architecture, termed MoS₂/NSCS. Systematic electrochemical measurements demonstrate that MoS₂/NSCS, when employed as the anode material in LIBs, exhibits a high capacity of 681 mA h g⁻¹ at 0.2 A g⁻¹ even after 110 cycles. The exceptional electrochemical performance of MoS₂/NSCS can be attributed to its unique porous 2D architecture. The few-layer MoS₂ sheets with a large interlayer distance reduce ion diffusion pathways and enhance ion mobility rates. Additionally, the N,S-doped porous carbon matrix not only preserves structural integrity but also facilitates electronic conductivity. These combined factors contribute to the reversible electrochemical activities observed in MoS₂/NSCS, highlighting its potential as a promising anode material for high-performance LIBs.

1. Introduction

The pressing societal demands underscore the rapid advancement of highly efficient energy storage and conversion technologies, such as lithium/sodium ion batteries (LIBs/SIBs), metal–air batteries, and proton exchange membrane fuel cells (PEMFCs).[1–3] LIBs, renowned for their high energy density, substantial power density, extended cycle life, minimal self-discharge, and environmental friendliness, hold immense promise for electric vehicles and renewable energy integration into the grid.[4–6] Despite significant progress achieved in enhancing LIB performance, there remains substantial scope for further improvement through the design of advanced nanostructured electrode materials. The structure and properties of both cathode and anode materials critically influence the energy and power densities of assembled LIBs.[7–9] Over recent decades, two-dimensional (2D) transition-metal dichalcogenides (MX₂, where M = Ti, V, Mo, W; and X = S or Se) have garnered considerable attention as high-performance anode materials for LIBs due to their advantageous physicochemical characteristics (*e.g.*, chemical, thermal, mechanical, and electrical properties).[10–13] The relatively large interlayer distance, approximately 0.62 nm along the lateral planes, facilitates

favorable diffusion pathways for ions during insertion/extraction cycles, thereby enhancing diffusion kinetics and specific capacities. MoS₂ materials, in particular, hold substantial practical potential for LIBs.[14–17] However, challenges such as inevitable volume changes and the poor intrinsic electrical and ionic conductivity inherent to two-dimensional MoS₂ often result in rapid capacity decay and inferior rate capability during charge/discharge cycles.

Several strategies have been proposed to mitigate or overcome the inherent challenges of MoS₂, such as integrating it with nanocarbons, shaping nanoscale morphologies and structures, and adjusting interlayer spacing.[18–21] Integration with advanced nanocarbons, particularly few-layer MoS₂ nanosheets, has shown improved electron and ion transport properties and enhanced stability during practical applications.[22–24] Various nanostructured carbon materials, encompassing sheets, tubes, cubes, fibers, and spheres, have been employed in combination with MoS₂.[23,25–27] Among these, two-dimensional (2D) carbon nanosheets are particularly promising due to their robust chemical stability, high electron conductivity, and excellent mechanical flexibility, making them ideal for electrochemical energy storage applications.[28,29] To date, MoS₂-2D nanocarbon composites, such as MoS₂/N-doped graphene,[30] MoS₂-graphene,[31] MoS₂/carbon framework,[32] graphene-wrapped MoS₂,[33] vertically aligned MoS₂/N-doped carbon nanosheets,[34] and MoS₂/graphene nanosheets,[35] have been developed for use in LIBs/SIBs, resulting in improved electrochemical performance. However, intrinsic challenges remain.[35–37] For instance, the tendency of 2D nanocarbons and

MoS_2 sheets to aggregate or restack can compromise performance during extended cycling and high-rate operation. Additionally, the loose interaction between few-layer MoS_2 and 2D nanocarbons can lead to significant contact resistance, thereby limiting rate capability and contributing to rapid capacity degradation.[26,27,38,39]

Addressing the intrinsic challenges of MoS_2/nanocarbon composite materials, embedding few-layer MoS_2 within porous carbon nanosheets holds significant promise for enhancing the storage performance of resulting LIBs. This approach offers dual benefits: firstly, it increases the electrode/electrolyte contact area, thereby improving storage capacity; secondly, it provides ample internal space to accommodate the volume changes during the reversible insertion and extraction of lithium ions.[28,40,41] Previous studies have predominantly reported MoS_2 layers stacked together with nanocarbon sheets, which inevitably impedes electronic transfer between them and promotes adverse reactions between MoS_2 and the electrolyte.[42–44] Consequently, these factors contribute to poor rate performance and rapid capacity degradation. These challenges underscore the urgent need for a reliable and effective approach to fabricate few-layer MoS_2 embedded within an advanced carbon matrix.

In this study, we present a straightforward and scalable approach for synthesizing a 2D architecture comprising *in situ* formed few-layer MoS_2 and N,S dual-doped carbon nanosheets (NSCS) through direct pyrolysis without requiring additional post-treatments. The nanosheet structure provides ample internal space to accommodate volume changes during repeated cycling, establishes a favorable network for rapid diffusion of electrolytes, and ensures continuous conductive pathways for efficient electron transfer. Leveraging these attributes, the MoS_2/NSCS composite, employed as anode materials for LIBs, demonstrates enhanced electrochemical performance characterized by high rate capability, large reversible capacity, and robust cycling durability.

2. Experiential section

2.1. Synthesis of MoS_2/NSCS

In a typical procedure, the ammonium molybdate, glucose, melamine, and L-cysteine with the calculated amount were dissolved into deionized water, then heated to evaporate the water. The obtained solid materials were calcinated at 900 °C under N_2 for 3 h with a heating rate of 10 °C min^{-1}. After the temperature was down to room temperature, the products were collected for further measurements.

2.2. Material characterization

X-ray diffraction (XRD) patterns of the samples were conducted on a Rigaku Smart Lab powder diffractometer at the voltage of 40 kV and current of 40 mA using Cu Kα radiation (λ = 1.5418 Å). The morphology and structure of the samples were investigated by using field emission scanning electron microscopy (FESEM, Jeol JSM-7500L), and transmission electron microscopy (TEM, Jeol JEM-2800). X-ray photoelectron spectroscopy (XPS) experiments were conducted on a Thermo Scientific ESCALAB 250Xi X-ray photoelectron spectrometer equipped with a monochromatic Al-Kα X-ray source (1486.6 eV). The surface area of the sample was calculated using a N_2 adsorption–desorption analyzer (Quantachrome Nove 2000e) based on the Brunauer–Emmett–Teller (BET) method. Raman spectra were recorded on a Thermo-Fisher Scientific DXR spectrometer (HORIBA, France) with 532 nm wavelength incident laser light.

2.3. Lithium-ion battery performance

The lithium-storage performance of the sample was measured by using CR2032 coin-type half cells. The working electrode includes 70 wt% of active material, 20 wt% of conductive carbon black, and 10 wt% of poly(vinyldifluoride) (PVDF). After fully stirring, the slurry was transferred in Cu foil and pasted using a blade. Before pressing, the electrodes were heated in a vacuum oven for 12 h in order to remove the organic solvent. Lithium foil was used as the counter electrode, glass microfiber (Whatman) was employed as the separator, and 1 M $LiPF_6$ in 1 : 1 (v/v) ethylene carbonate/dimethyl carbonate was worked as electrolyte. Cyclic voltammetry (CV) was collected on a Zennium IM6eX (Zahner, Germany) electrochemical workstation. And galvanostatic charge/discharge performance was tested on a LAND CT2001A system.

3. Results and discussion

High-crystalline MoS_2 embedded into heteroatom-doped carbon nanosheets (MoS_2/NSCS) was synthesized *via* a one-pot pyrolysis process involving a mixture of ammonium molybdate, glucose, melamine, and L-cysteine, as depicted in Fig. 1. During the process, glucose acts as the carbon source and decomposes around 300 °C, subsequently carbonizing to form carbon sheets. Ammonium molybdate, serving as the Mo source, reacts with sublimated sulfur from sulfydryl-groups of L-cysteine as the temperature increases, thereby facilitating the formation of few-layer MoS_2 on the carbon sheets.[25,45] The presence of sufficient tri-striazine units in melamine ensures successful doping of nitrogen into the resulting carbon framework.[46,47]

The crystalline phases of the synthesized materials were characterized using powder X-ray diffraction (XRD) and Raman spectroscopy. Fig. S1a† displays the XRD pattern of MoS_2/NSCS, revealing sharp diffraction peaks that correspond to the typical planes of hexagonal MoS_2 crystalline structure (JCPDS No. 65-1951). The dominant peak observed at 14.4° (2θ) is assigned to the (002) plane of MoS_2, indicating well-developed growth of the MoS_2 (002) crystalline plane, which is favorable for the insertion and extraction of lithium ions during electrochemical processes. Fig. S1† shows the Raman spectrum of MoS_2/NSCS, where two characteristic peaks are observed at approximately 1358 cm^{-1} (D band) and 1594 cm^{-1} (G band), corresponding to the typical features of carbonaceous materials. The intensity ratio of the D and G bands is measured as 1.07 for MoS_2/NSCS, indicating a higher level of structural defects or disorder within the MoS_2/NSCS nanocomposite. This structural disorder is
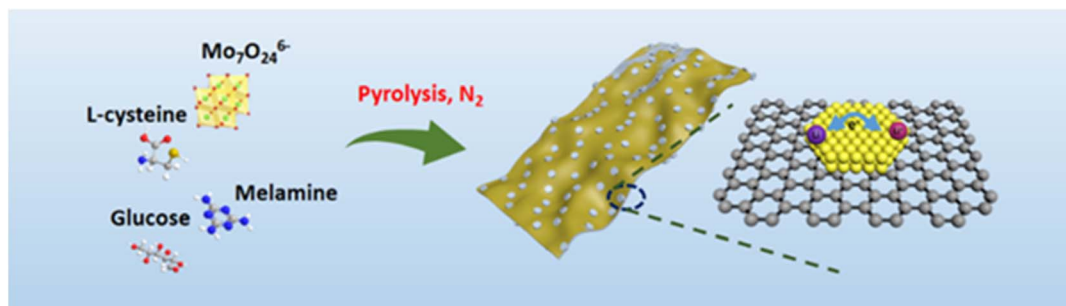
Fig. 1 Schematic illustration of the synthetic procedure of MoS$_2$/NPCS.

beneficial for improving the electrical performance of the material. Additionally, weakened peaks observed at around 380 cm^{-1} and 410 cm^{-1} are attributed to the in-plane E^1_{2g} and the out-of-plane A_{1g} vibrations of MoS$_2$, respectively. Overall, the XRD pattern and Raman spectra collectively confirm the formation of MoS$_2$ and its incorporation into a defected carbon nanocomposite structure.

The micro-morphology and nano-structure of the MoS$_2$/NSCS composite were characterized using scanning electron microscopy (SEM), and transmission electron microscopy (TEM). In Fig. 2a, the SEM image clearly shows the well-organized nanosheet structure of MoS$_2$/NSCS. Upon further magnification (Fig. 2b), random nanopores are observed on the interwoven nanosheets, highlighting the porous nature of the material. TEM images in Fig. 2c and d depict cross-linked nanosheets that form an interconnected network, emphasizing the porous morphology of the nanosheets. This integrated 2D architecture comprising few-layer MoS$_2$ sheets and porous carbon nanosheets offers abundant and accessible active sites, as well as short diffusion paths for lithium ions.

Fig. 2e shows the HR-TEM image with visible interlayer spacing of approximately 0.62 nm, corresponding to the (002) crystalline plane of MoS$_2$, and an interatomic distance of 0.27 nm, assigned to the (100) plane of hexagonal MoS$_2$. The larger interlayer spacing of the few-layer MoS$_2$ sheets facilitates the reversible insertion and extraction of lithium ions during charge/discharge cycles. Fig. 2f presents the EDS mapping of MoS$_2$/NSCS, demonstrating a homogeneous distribution of C, Mo, S, and N elements throughout the material. This confirms the intimate connection between the MoS$_2$ and carbon matrix, highlighting the successful synthesis of MoS$_2$/NSCS with integrated elemental distribution and structural integrity.

N$_2$ adsorption–desorption isotherms were utilized to characterize the surface area and porous structure of the MoS$_2$/NSCS composite. In Fig. 3a, the isotherm exhibits a typical hysteresis loop, indicating the presence of a porous architecture within the material. The Brunauer–Emmett–Teller (BET) surface area of MoS$_2$/NSCS is determined to be 117 m^2 g^{-1}. Furthermore, the Barrett–Joyner–Halenda (BJH) method, shown in the inset of Fig. 3a, reveals a pore size distribution ranging from micropores
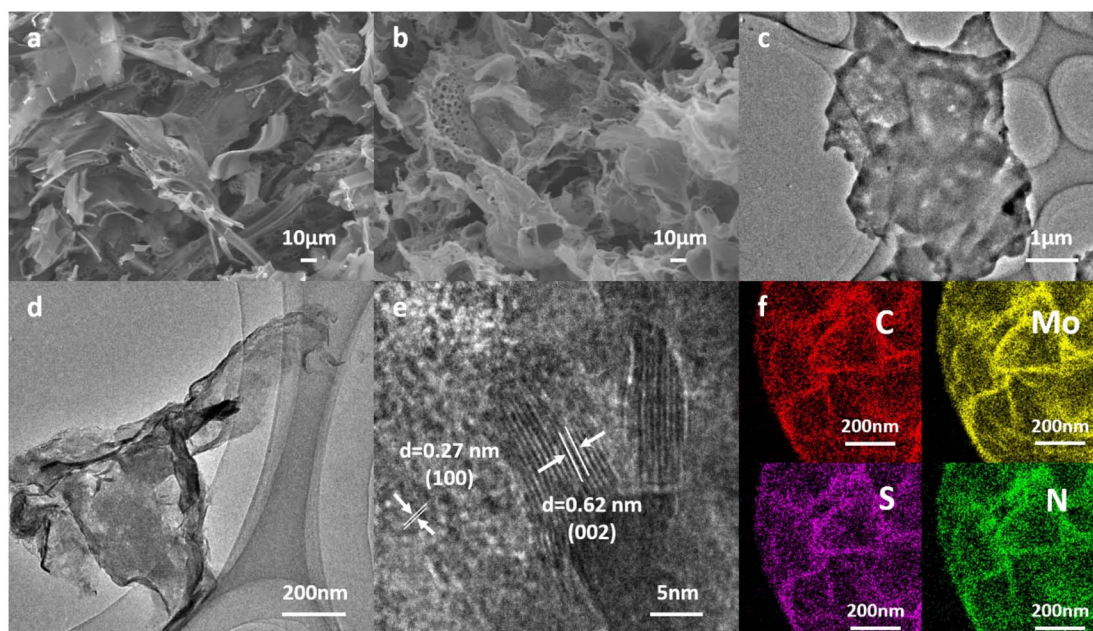

Fig. 2 (a and b) SEM, (c and d) TEM, (e) HR-TEM images of MoS$_2$/NSCS. (f) Element mapping of MoS$_2$/NSCS.
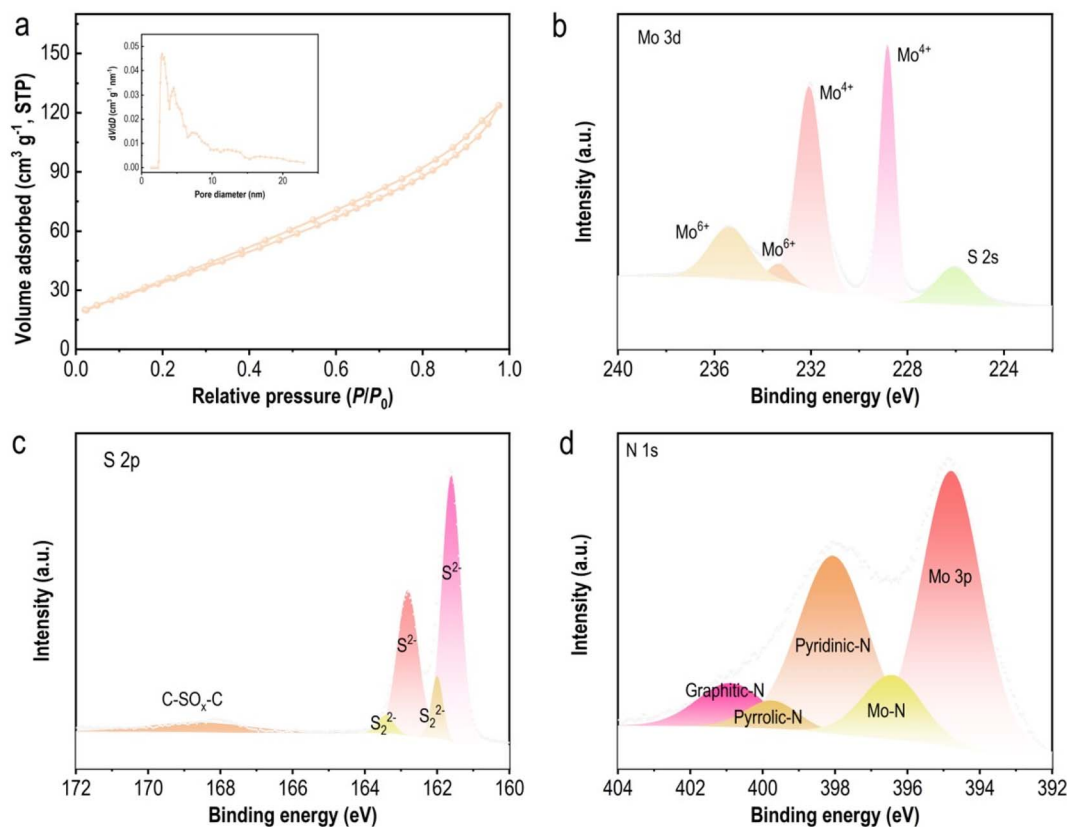
Fig. 3 (a) N_2 adsorption–desorption isotherms of MoS$_2$/NSCS. The inset presents the corresponding pore size distribution. High-resolution XPS Mo 3d (b), S 2p (c), and N 1s (d) spectra of MoS$_2$/NSCS.

to mesopores (1–26 nm). This hierarchical porous structure is advantageous as it provides ample pathways for electrolyte diffusion, thereby shortening diffusion paths. Moreover, these pores offer sufficient space to accommodate volume changes during the intercalation–deintercalation processes of lithium ions, contributing to the material's stability and electrochemical performance in battery applications.

X-ray photoelectron spectroscopy (XPS) measurements were conducted to analyze the surface chemical composition and bonding states of MoS$_2$/NSCS. The XPS survey scan (Fig. S2a†) confirms the presence of C, O, N, S, and Mo elements on the material surface. The C 1s spectrum (Fig. S2b†) reveals four distinct peaks at 284.8, 286.3, 287.9, and 290.3 eV, corresponding to C=C/C–C, C–S/C–N/C=O, C–CO$_3$, and π–π*, respectively.[48,49] These peaks indicate the presence of carbon species within the MoS$_2$/NSCS composite, including contributions from carbon–carbon bonds, carbon–sulfur/nitrogen/oxygen bonds, carbonate species, and π-electron systems. The Mo 3d spectrum (Fig. 3b) exhibits peaks centered at 228.8 and 232.1 eV, corresponding to Mo 3d$_{5/2}$ and Mo 3d$_{3/2}$ of Mo^{4+} in MoS$_2$. Additionally, peaks at 232.2 and 235.9 eV indicate the presence of Mo^{6+} species likely arising from surface molybdenum oxides formed upon exposure to air.[50,51] The Mo 3d spectrum also includes a smaller peak at 226.1 eV, corresponding to S 2s peak. In the S 2p spectrum (Fig. 3c), peaks at 161.6 and 162.8 eV correspond to apical S^{2-} and basal plane S^{2-},

respectively, while peaks at 162.0 and 163.4 eV are attributed to bridging S$_2^{2-}$ and terminal S$_2^{2-}$ species. These peaks confirm the presence of divalent sulfide ions within the MoS$_2$ structure.[32,52] Additionally, the broad peak at 168.4 eV indicates the presence of C–SO$_x$–C species, confirming the incorporation of sulfur into the carbonaceous skeleton. The high-resolution N 1s spectrum (Fig. 3d) shows peaks at 397.9 eV (pyridinic N), 399.7 eV (pyrrolic N), and 400.8 eV (graphitic N), indicating the presence of nitrogen species within the MoS$_2$/NSCS composite.[53,54] The total nitrogen content is measured to be 4.7 at%. Moreover, the Mo 3p peak at 394.7 eV and Mo–N peak at 396.5 eV demonstrate a strong coupling effect between MoS$_2$ and the carbon matrix, which influences the structural and electronic properties of MoS$_2$, ultimately enhancing its performance as a lithium storage material in batteries.

Lithium-ion batteries (LIBs) have garnered considerable attention due to their high operating voltage, significant energy density, and extended cycle life. MoS$_2$-based materials, leveraging their unique interlayer structure, hold substantial promise as anodes for LIBs.[19,28,55] The expanded interlayer spacing in MoS$_2$ materials plays a crucial role in mitigating volume expansion during charge–discharge cycles, thereby enhancing cycling stability. Here, MoS$_2$@NSCS was evaluated as an anode material for LIBs storage. Fig. 4a depicts the cyclic voltammetry (CV) curves of MoS$_2$@NSCS recorded at a scan rate of 0.2 mV s^{-1}. In the initial cycle, a reduction peak appears
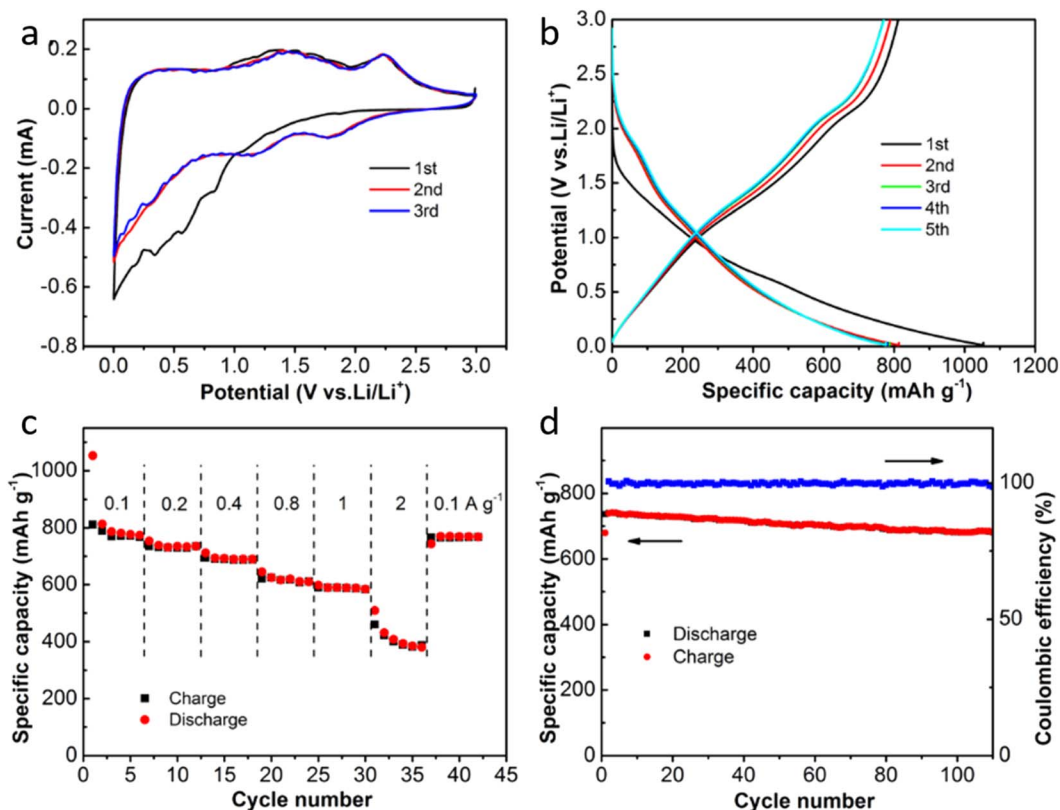
Fig. 4 Electrochemical performance of the MoS$_2$/NSCS in LIBs. (a) CV curves of the MoS$_2$@NSCS at a scan rate of 0.2 mV s^{-1}. (b) Galvanostatic discharge–charge profiles of the MoS$_2$@NSCS for five cycles at a current density of 0.1 A g^{-1}. (c) Rate performance of MoS$_2$@NSCS at different current densities. (d) Cycling behaviors of MoS$_2$@NSCS at 0.2 A g^{-1} between 0.0 and 3.0 V.

around 0.8–0.3 V (*vs.* Li$^+$/Li), attributed to the formation of a solid electrolyte interphase (SEI) as lithium ions intercalate into the MoS$_2$ interlayers. This irreversible capacity loss is typical during the initial discharging–charging process.[56,57] Subsequent cycles show the disappearance of this reduction peak and the emergence of new reduction peaks at approximately 1.78, 1.16, and 0.30 V, corresponding to the formation of Li$_2$S, Li$_x$MoS$_2$, and the decomposition of lithiated MoS$_2$, respectively, consistent with previous reports.[53,58] During the anodic stage, oxidation peaks at approximately 1.42 and 2.22 V are observed, corresponding to the oxidation of Mo to form MoS$_2$ and the production of sulfur, respectively.[47,57] The nearly overlapping CV curves in the subsequent cycles indicate excellent reversibility of the electrochemical reactions. Fig. 4b presents the galvanostatic charging–discharging profiles of MoS$_2$@NSCS over five cycles at a current density of 0.2 A g^{-1}. A distinct voltage plateau at around 0.7 V is observed during the initial discharging process, associated with SEI formation and electrolyte decomposition. This plateau diminishes in subsequent cycles.[32,53] Voltage plateaus at approximately 2.2 V and 1.2 V in subsequent cycles correspond to the reversible deintercalation and intercalation of lithium ions, consistent with the CV results.

The galvanostatic discharging–charging profiles of MoS$_2$@NSCS at various current densities within the 0.0–3.0 V voltage range illustrate its impressive electrochemical performance, as

shown in Fig. S3.† Across current densities ranging from 0.1 to 2 A g^{-1}, the MoS$_2$@NSCS electrode exhibits well-defined discharge–charge curves, indicative of excellent reversibility. In Fig. 4c, the specific capacities decrease gradually from approximately 781 mA h g^{-1} at 0.1 A g^{-1} to 382 mA h g^{-1} at 2 A g^{-1}. This performance is comparable to other reported MoS$_2$-based materials with varying configurations for LIBs, as summarized in Table S1.† Upon returning to 0.1 A g^{-1}, the electrode retains a capacity of 766 mA h g^{-1}, demonstrating remarkable rate capability. Long-term cycling stability was also assessed at a current density of 0.2 A g^{-1} (Fig. 4d), revealing outstanding durability of MoS$_2$@NSCS. After 110 cycles, the electrode maintains a high capacity of 681 mA h g^{-1}, underscoring its robust performance under high-rate cycling conditions. This exceptional electrochemical performance can be attributed to several key factors: the hierarchically porous nanosheet structure, the excellent conductivity of the carbon substrate, the high storage capacity of MoS$_2$ nanosheets, and the strong interaction between the carbon substrate and MoS$_2$ sheets. The unique sheet-on-sheet architecture of MoS$_2$@NSCS facilitates strong interactions that stabilize the integrated structure and inhibit the exfoliation of MoS$_2$ nanosheets during lithiation and delithiation processes. This structure promotes fast electron transport and ensures superior long-term durability during charge–discharge cycles. Overall, these attributes

highlight MoS_2@NSCS as a promising candidate for high-performance lithium-ion battery applications.

4. Conclusions

This work provides the universal and scalable approach for developing well-designed 2D porous structure with uniformly dispersed few-layer MoS_2 sheets and heteroatoms-modified carbon nanosheets as the advanced electrodes for enhancing the performance of LIBs. This one-step and *in situ* sulfurization strategy without any post-treatments of the organic precursor achieves the strong coupling interaction between MoS_2 sheets and porous carbon nanosheets in the resultant nanocomposite materials. Furthermore, as anode materials for LIBs, the large specific capacity (780 mA h g^{-1} at 0.1 A g^{-1}) and robust stability (no evident decay after 110 cycles at 0.2 A g^{-1}) are both obtained for MoS_2/NSCS electrode. Such LIBs performance of the fabricated MoS_2/NSCS material is comparable to most of reported active MoS_2-based materials with different configuration. The hierarchical structures with intimate coupled ultrathin carbon nanosheets and well-organized MoS_2 sheets are responsible for the outstanding electrochemical performance of the fabricated MoS_2/NSCS materials. The present work is expected to provide some novel inspiration to develop the functional materials with intimate interaction between different components for electrochemical reactions and other energy-related fields.

Data availability

Data are available upon request from the authors. The data supporting this article have been included as part of the ESI.†

Conflicts of interest

The authors have no conflicts of interest to declare.

Acknowledgements

References

1 Y. Huang, M. Zhu, Y. Huang, Z. Pei, H. Li, Z. Wang, Q. Xue and C. Zhi, *Adv. Mater.*, 2016, **28**, 8344–8364.

2 J.-T. Ren, L. Chen, H.-Y. Wang, Y. Feng and Z.-Y. Yuan, *Energy Environ. Sci.*, 2024, **17**, 3960–4009.

3 C. Liu, Q. Lu, M. V. Gorbunov, A. Omar, I. G. Gonzalez Martinez, P. Zhao, M. Hantusch, A. Dimas Chandra Permana, H. He, N. Gaponik and D. Mikhailova, *J. Energy Chem.*, 2023, **79**, 373–381.

4 C. Liu, F. Li, L. P. Ma and H. M. Cheng, *Adv. Mater.*, 2010, **22**, E28–E62.

5 X. Luo, J. Wang, M. Dooner and J. Clarke, *Appl. Energy*, 2015, **137**, 511–536.

6 E. Talaie, P. Bonnick, X. Sun, Q. Pang, X. Liang and L. F. Nazar, *Chem. Mater.*, 2017, **29**, 90–105.

7 P. G. Bruce, B. Scrosati and J. M. Tarascon, *Angew. Chem., Int. Ed.*, 2008, **47**, 2930–2946.

8 J. B. Goodenough and Y. Kim, *Chem. Mater.*, 2010, **22**, 587–603.

9 V. Etacheri, R. Marom, R. Elazari, G. Salitra and D. Aurbach, *Energy Environ. Sci.*, 2011, **4**, 3243–3262.

10 Z. Yang, J. Zhang, M. C. W. Kintner-Meyer, X. Lu, D. Choi, J. P. Lemmon and J. Liu, *Chem. Rev.*, 2011, **111**, 3577–3613.

11 J. M. Tarascon and M. Armand, *Nature*, 2001, **414**, 359–367.

12 A. S. Aricò, P. Bruce, B. Scrosati, J. M. Tarascon and W. Van Schalkwijk, *Nat. Mater.*, 2005, **4**, 366–377.

13 E. Pomerantseva and Y. Gogotsi, *Nat. Energy*, 2017, **2**, 17089.

14 X. Huang, Z. Zeng and H. Zhang, *Chem. Soc. Rev.*, 2013, **42**, 1934–1946.

15 T. Stephenson, Z. Li, B. Olsen and D. Mitlin, *Energy Environ. Sci.*, 2014, **7**, 209–231.

16 M. Chhowalla, H. S. Shin, G. Eda, L. J. Li, K. P. Loh and H. Zhang, *Nat. Chem.*, 2013, **5**, 263–275.

17 H. Hwang, H. Kim and J. Cho, *Nano Lett.*, 2011, **11**, 4826–4830.

18 J. Xiao, X. Wang, X. Q. Yang, S. Xun, G. Liu, P. K. Koech, J. Liu and J. P. Lemmon, *Adv. Funct. Mater.*, 2011, **21**, 2840–2846.

19 Y. Wang, Q. Qu, G. Li, T. Gao, F. Qian, J. Shao, W. Liu, Q. Shi and H. Zheng, *Small*, 2016, **12**, 6033–6041.

20 D. Xie, X. Xia, Y. Wang, D. Wang, Y. Zhong, W. Tang, X. Wang and J. Tu, *Chem.–Eur. J.*, 2016, **22**, 11617–11623.

21 Q. Lu, C. Liu, Y. Zhao, W. Pan, K. Xie, P. Yue, G. Zhang, A. Omar, L. Liu, M. Yu and D. Mikhailova, *SusMat*, 2023, **3**, 471–497.

22 J. Kong, C. Zhao, Y. Wei and X. Lu, *ACS Appl. Mater. Interfaces*, 2015, **7**, 24279–24287.

23 J. Zhou, J. Qin, X. Zhang, C. Shi, E. Liu, J. Li, N. Zhao and C. He, *ACS Nano*, 2015, **9**, 3837–3848.

24 J. T. Ren, L. Chen, D. D. Yang and Z. Y. Yuan, *Appl. Catal., B*, 2020, **263**, 118352.

25 Y. Chao, R. Jalili, Y. Ge, C. Wang, T. Zheng, K. Shu and G. G. Wallace, *Adv. Funct. Mater.*, 2017, **27**, 1700234.

26 S. Xia, Y. Wang, Y. Liu, C. Wu, M. Wu and H. Zhang, *Chem. Eng. J.*, 2018, **332**, 431–439.

27 J. Wang, J. Liu, D. Chao, J. Yan, J. Lin and Z. X. Shen, *Adv. Mater.*, 2014, **26**, 7162–7169.

28 X. Y. Yu, H. Hu, Y. Wang, H. Chen and X. W. D. Lou, *Angew. Chem., Int. Ed.*, 2015, **54**, 7395–7398.

29 F. Zhou, S. Xin, H. W. Liang, L. T. Song and S. H. Yu, *Angew. Chem., Int. Ed.*, 2014, **53**, 11552–11556.

30 J. Su, G.-D. Li, X.-H. Li and J.-S. Chen, *Adv. Sci.*, 2019, **6**, 1801702.

31 L. Zhang, H. B. Wu, Y. Yan, X. Wang and X. W. Lou, *Energy Environ. Sci.*, 2014, **7**, 3302–3306.

32 Y. Fang, Y. Lv, F. Gong, A. A. Elzatahry, G. Zheng and D. Zhao, *Adv. Mater.*, 2016, **28**, 9385–9390.

33 X. Hu, Y. Li, G. Zeng, J. Jia, H. Zhan and Z. Wen, *ACS Nano*, 2018, **12**, 1592–1602.

34 Z.-H. Zhao, X.-D. Hu, H. Wang, M.-Y. Ye, Z.-Y. Sang, H.-M. Ji, X.-L. Li and Y. Dai, *Nano Energy*, 2018, **48**, 526–535.

35 D. Sun, D. Ye, P. Liu, Y. Tang, J. Guo, L. Wang and H. Wang, *Adv. Energy Mater.*, 2018, **8**, 1702383.

36 S. Anwer, Y. Huang, B. Li, B. Govindan, K. Liao, J. C. W, F. Wu, R. Chen and L. Zheng, *ACS Appl. Mater. Interfaces*, 2019, **11**, 22323–22331.

37 M. Zhen, J. Wang, S.-q. Guo and B. Shen, *Appl. Surf. Sci.*, 2019, **487**, 285–294.

38 X. Xie, Z. Ao, D. Su, J. Zhang and G. Wang, *Adv. Funct. Mater.*, 2015, **25**, 1393–1403.

39 H. Wang, D. Ren, Z. Zhu, P. Saha, H. Jiang and C. Li, *Chem. Eng. J.*, 2016, **288**, 179–184.

40 Z. Li, A. Ottmann, T. Zhang, Q. Sun, H. P. Meyer, Y. Vaynzof, J. Xiang and R. Klingeler, *J. Mater. Chem. A*, 2017, **5**, 3987–3994.

41 T. S. Sahu, Q. Li, J. Wu, V. P. Dravid and S. Mitra, *J. Mater. Chem. A*, 2017, **5**, 355–363.

42 B. Guo, K. Yu, H. Song, H. Li, Y. Tan, H. Fu, C. Li, X. Lei and Z. Zhu, *Nanoscale*, 2016, **8**, 420–430.

43 J. Shao, Q. Qu, Z. Wan, T. Gao, Z. Zuo and H. Zheng, *ACS Appl. Mater. Interfaces*, 2015, **7**, 22927–22934.

44 L. David, R. Bhandavat and G. Singh, *ACS Nano*, 2014, **8**, 1759–1770.

45 K. Chang, D. Geng, X. Li, J. Yang, Y. Tang, M. Cai, R. Li and X. Sun, *Adv. Energy Mater.*, 2013, **3**, 839–844.

46 H. Wang, Y. Cao, C. Sun, G. Zou, J. Huang, X. Kuai, J. Zhao and L. Gao, *ChemSusChem*, 2017, **10**, 3540–3546.

47 K. Chang and W. Chen, *ACS Nano*, 2011, **5**, 4720–4728.

48 J. T. Ren and Z. Y. Yuan, *ACS Sustainable Chem. Eng.*, 2019, **7**, 10121–10131.

49 Y. P. Zhu, Y. L. Liu, Y. P. Liu, T. Z. Ren, G. H. Du, T. H. Chen and Z. Y. Yuan, *J. Mater. Chem. A*, 2015, **3**, 11725–11729.

50 J. T. Ren and Z. Y. Yuan, *J. Mater. Chem. A*, 2019, **7**, 13591–13601.

51 J. T. Ren, G. G. Yuan, C. C. Weng, L. Chen and Z. Y. Yuan, *ChemCatChem*, 2018, **10**, 5297–5305.

52 J. T. Ren and Z. Y. Yuan, *ChemCatChem*, 2018, **10**, 3260–3268.

53 B. Sun, Q. Liu, W. Chen, N. Wang, J. Gu, W. Zhang, H. Su and D. Zhang, *J. Mater. Chem. A*, 2018, **6**, 6289–6298.

54 J. Shao, T. Gao, Q. Qu, Q. Shi, Z. Zuo and H. Zheng, *J. Power Sources*, 2016, **324**, 1–7.

55 J. T. Ren, L. Chen, C. C. Weng, G. G. Yuan and Z. Y. Yuan, *ACS Appl. Mater. Interfaces*, 2018, **10**, 33276–33286.

56 Y. Wang, D. Kong, W. Shi, B. Liu, G. J. Sim, Q. Ge and H. Y. Yang, *Adv. Energy Mater.*, 2016, **6**, 1601057.

57 J. Ren, R.-P. Ren and Y.-K. Lv, *Chem. Eng. J.*, 2018, **353**, 419–424.

58 Y. Ge, C. Wang, Y. Zhao, Y. Liu, Y. Chao, T. Zheng and G. G. Wallace, *Small*, 2018, **14**, 1703096.

© 2024 The Author(s). Published by the Royal Society of Chemistry